

# Solution Structure of an Amyloid-Forming Protein During Photoinitiated Hexamer–Dodecamer Transitions Revealed through Small-Angle Neutron Scattering<sup>†</sup>

Andrea C. Hamill, Shao-Chun Wang, and C. Ted Lee, Jr.\*

Department of Chemical Engineering and Materials Science, University of Southern California, Los Angeles, California 90089-1211

Received February 2, 2007; Revised Manuscript Received April 18, 2007

**ABSTRACT:** Shape-reconstruction analysis applied to small angle neutron scattering (SANS) data is used to determine the in vitro conformations of  $\alpha$ -chymotrypsin oligomers that form as a result of partial unfolding with a photoresponsive surfactant. In the presence of the photoactive surfactant under visible light, the native oligomers (dimers or compact hexamers) rearrange into expanded corkscrew-like hexamers. Converting the surfactant to the photopassive form with UV light illumination causes the hexamers to laterally aggregate and intertwine into dodecamers with elongated, twisted conformations containing cross-sectional dimensions similar to amyloid protofilaments. Secondary-structure measurements with FT-IR indicate that this photoinduced hexamer-to-dodecamer association occurs through intermolecular  $\beta$  sheets stabilized with hydrogen bonds, similar to amyloid formation. Traditional structural characterization techniques such as X-ray crystallography and NMR are not easily amenable to the study of these non-native protein conformations; however, SANS is ideally suited to the study of these associated intermediates, providing direct observation of the mechanism of oligomeric formation in an amyloid-forming protein. Combined with photoinitiated hexamer-to-dodecamer associations in the presence of the photoresponsive surfactant, this study could provide unique insight into the amyloidosis disease pathway, as well as novel disease treatment strategies.

Proteins interact with a variety of molecules during the course of activity, ranging from small ions and ligands to other proteins through either heterogeneous or homogeneous association. Indeed, the dynamic and multifarious response of proteins to these interactions is utilized to stimulate or regulate virtually every biological process. In some cases, however, protein interactions can result in unwanted or deleterious effects, such as protein–protein associations leading to amyloid fibril formation. The most well-known example of this process involves the aggregation of the amyloid- $\beta$  ( $A\beta$ )<sup>1</sup> peptide fragments  $A\beta$ 40 and  $A\beta$ 42 implicated in Alzheimer's disease, although amyloid fibrils have been observed in an array of proteins largely independent of the native secondary structure (1), including ribonuclease A (2), an SH3 domain, lysozyme (3), insulin (4), and  $\alpha$ -chymotrypsin (5). This process is generally believed to result from the formation of unstable slightly unfolded

conformations, leading to a cascading aggregation process from *monomers* to *oligomers* [unstructured aggregates of typically multiples of six molecules in the case of  $A\beta$ 42(6)] to *protofibrils* (structured aggregates exhibiting  $\beta$ -sheet structure) to *protofilaments* (elongated aggregates  $\sim$ 2–5 nm in diameter) to *fibrils* (2–6 entwined protofilaments) (1). Perhaps most importantly, the prefibrillar intermediates (i.e., oligomers and protofibrils), which can induce cognitive impairment, have become increasingly viewed as the primary pathogenic species (1, 7).

To date, however, the solution structure of these important intermediate species remains unknown as the two preferred methods to determine protein structure, namely, X-ray crystallography and solution NMR, are generally limited to the study of native proteins in the solid state or relatively small protein assemblies, respectively, since protein crystallization is often supplanted by unwanted aggregation and crystal-packing constraints largely dominate protein orientations in multimolecular complexes. Thus, the development of novel structural characterization methods capable of examining *partially folded proteins* in non-native conformations and *supramolecular complexes* undergoing self- or heteroassociation is highly desired. For example, through the use of small-angle neutron scattering (SANS), the in vitro structures of  $A\beta$ 40 protofibrils were found to be cylindrical with 24 Å cross-sectional radii and 110 Å long (8), while through AFM and TEM measurements a variety of protofibril arrangements have been observed, including twisted chains

<sup>†</sup> This material is based upon work supported by the National Science Foundation under Grant No. 0554115.

\* To whom correspondence should be addressed. Phone: (213) 740-2066. Fax: (213) 740-8053. E-mail: tedlee@usc.edu.

<sup>1</sup> Abbreviations:  $A\beta$ , amyloid  $\beta$ ;  $\alpha$ -Ch,  $\alpha$ -chymotrypsin; AFM, atomic force microscopy; azoTAB, azobenzenetrimethylammonium bromide; BSA, bovine serum albumin; FSD, Fourier self-deconvolution; FT-IR, Fourier transform infrared spectroscopy; NIST, National Institute of Standards and Technology; NMR, nuclear magnetic resonance spectroscopy; PDB, Protein Data Bank; PDDF, pair distance distribution function; SANS, small-angle neutron scattering; SAXS, small-angle X-ray scattering; TEM, transmission electron microscopy; TFE, trifluoroethanol; UV, ultraviolet.

2–5 nm in diameter. However, due to the relatively low resolution of the cylindrical models employed in the above SANS analysis, combined with potential influences of surface interactions with AFM and TEM, the precise conformation of protofibrils in solution remains unknown. As a result, to properly investigate intermediate conformations in an amyloid protein necessitates two complementary approaches: (1) a means to induce changes in protein folding and, hence, association in a controlled and preferably reversible manner and (2) a method to determine the conformation of non-native and associated proteins at relatively high resolution.

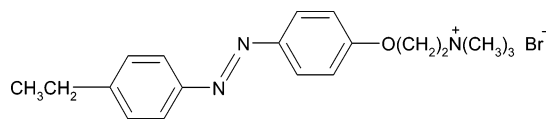
Recently, we have shown that light illumination can be used to induce photoreversible changes in both the secondary (9) and tertiary (10, 11) structure of proteins. This method utilizes the interaction of proteins with photosensitive “azoTAB” surfactants containing an azobenzene group that undergoes a *trans* (relatively hydrophobic) to *cis* (relatively hydrophilic) photoisomerization upon exposure to visible (434 nm) or UV (350 nm) light illumination, respectively. Hence, light can be used to reversibly bind the surfactant to the hydrophobic domains of proteins, leading to photocontrol of protein folding. Furthermore, we have applied small-angle neutron scattering (SANS) to study the *in vitro* structure of the non-native protein conformations that form in response to photosurfactant and light. Small-angle neutron and X-ray scattering have been used for several decades to investigate the structure of soluble proteins in solution (12–15) and membrane proteins in surfactant assemblies (16, 17). The obtained structures have typically been low resolution, however, a consequence of modeling proteins with a single dimension (radius of gyration) or as ellipsoids (axial radii). These procedures, although convenient, belie the wealth of structural information contained within the measured scattering intensity. From the range of momentum vectors  $Q = 4\pi\lambda^{-1} \sin(\theta/2)$ , where  $\lambda$  is the neutron wavelength (6 Å) and  $\theta$  is the scattering angle, in a typical SANS experiment ( $Q = 0.005\text{--}0.5 \text{ \AA}^{-1}$ ), it can be seen that the data span length scales ( $L = 2\pi/Q$ ) ranging from 12.5 to 1250 Å, ideal for protein conformational studies. Indeed, application of shape-reconstruction techniques such as the *ab initio* methods of GASBOR (14) and GA\_STRUCT (15) reveals a high degree of similarity between the *native* structure in solution (SANS) and in the solid state (X-ray crystallography), a seemingly general property of soluble proteins (12).

In the present study, the ability to photoinitiate changes in protein quaternary structure through photocontrol of  $\alpha$ -chymotrypsin self-association is demonstrated. Native  $\alpha$ -chymotrypsin is well-known to self-associate through either a monomer–dimer (pH 3) or monomer–hexamer (pH 7) equilibrium, while the addition of trifluoroethanol, a solvent known to induce partially folded structures (18, 19), has been reported to result in  $\alpha$ -chymotrypsin amyloid-fibril formation (5). Mixing  $\alpha$ -chymotrypsin with the photoreversible azoTAB surfactant is found to result in partial unfolding of the protein, giving rise to changes in both the degree and type of self-association. Shape-reconstruction analysis applied to SANS data allows determination of the *in vitro* conformation of  $\alpha$ -chymotrypsin oligomers. In the presence of azoTAB under visible light, native oligomers (dimer or compact hexamers) are converted to expanded corkscrew-like hexamers, while upon UV light illumination

the hexamers laterally aggregate, wrapping around each other to form dodecamers with twisted conformations. FT-IR measurements of the protein secondary structure reveal that dodecamer formation is accompanied by hydrogen bond stabilized intermolecular  $\beta$  sheets, commonly observed in amyloid fibrils. TEM measurements following incubation further confirm the formation of fibrillar structures, while photocontrol of the hexamer-to-dodecamer association process is studied with small-angle X-ray scattering (SAXS) measurements. Together, these results provide the first direct observation of the mechanism of formation of the key intermediates in an amyloid-forming protein, which could provide unique insight into the amyloidosis disease pathway.

## EXPERIMENTAL PROCEDURES

An azobenzenetrimethylammonium bromide surfactant (azoTAB) of the form



similar to surfactants used in previous studies (9–11, 20) was synthesized according to published procedures (21, 22). When illuminated with 350 nm UV light, the surfactant undergoes a photoisomerization predominantly to the *cis* form (90/10 *cis/trans*), which can be rapidly reversed upon exposure to visible light (434 nm, 75/25 *trans/cis*) or in the dark in about 24 h ( $\sim 100\%$  *trans* isomer) (23). For the SAXS and FT-IR measurements, conversion to the UV light form was achieved with the 365 nm line from a 200 W mercury arc lamp (Oriel, model 6283), isolated with the combination of a 320 nm band-pass filter (Oriel, model 59800) and an IR filter (Oriel, model 59060). A 400 nm long-pass filter (Oriel, model 59472) was used to convert back to the visible light form. In the SANS experiments, the solutions were exposed to an 84 W long-wave UV lamp (365 nm; Spectroline, model XX-15A) for at least 30 min prior to sample collection to convert to the UV light form and were continuously exposed to the same UV light throughout the data collection.

Type II, essentially salt-free  $\alpha$ -chymotrypsin from bovine pancreas (Sigma, catalog number C-4129, lot 105K7670), 5 $\times$  crystallized chymotrypsinogen-A from bovine pancreas (Worthington, catalog number LS005630), and phosphate buffer (Sigma, catalog number P-3288, pH 7.2, 8.3 mM) were used as received. All other chemicals were obtained from Aldrich in the highest purity. For the experiments performed at pH 3, HCl (37%) was added to the pH 7.2 buffer as needed.

Small-angle neutron scattering experiments were performed on the 30 m NG3 SANS instrument at NIST (24). A neutron wavelength of  $\lambda = 6 \text{ \AA}$  and a detector offset of 25 cm with two sample-detector distances of 1.33 and 7.0 m were utilized to achieve a  $Q$  range of 0.0048–0.46  $\text{\AA}^{-1}$ . The net intensities were corrected for the background and empty cell (pure D<sub>2</sub>O), accounting for the detector efficiency using the scattering from an isotropic scatterer (Plexiglas), and converted to an absolute differential cross section per unit sample volume (in units of  $\text{cm}^{-1}$ ) using an attenuated

empty beam. The data were then corrected for incoherent scattering by subtracting a constant background. The shape-reconstruction algorithm GA\_STRUCT (15) was used to generate solution conformations, similar to previous studies (10, 11). Beginning with an initial guess of randomly distributed scattering centers, the program rearranges the position of the scattering centers to best fit the experimental scattering data.

The weight-average molecular weight ( $M_w$ ) of each sample was calculated from the equation

$$M_w = \frac{1000I(0)N_A}{c\bar{v}^2(\rho_p - \rho_s)^2} \quad (1)$$

where  $\rho_s$  and  $\rho_p$  are the scattering length densities of the solvent ( $6.36 \times 10^{10} \text{ cm}^{-2}$ ) and protein ( $3.23 \times 10^{10} \text{ cm}^{-2}$ ), respectively,  $c$  is the protein concentration (11.6 mg/mL at pH 3 and 11.4 mg/mL at pH 7), and  $\bar{v}$  is the protein specific volume ( $0.734 \text{ cm}^3/\text{g}$ ) (25).  $I(0)$  values were determined from Guinier plots (25) using  $I(Q) = I(0) \exp(-Q^2 R_g^2/3)$ , where  $R_g$  is the radius of gyration. Guinier plots, generally valid for  $QR_g < 1.3$ , can be influenced by solution structuring due to intermolecular interactions between charged proteins, which becomes increasingly important as  $Q$  decreases below  $1.5/R$  (10) (or  $<0.05 \text{ \AA}^{-1}$  using an  $\alpha$ -Ch radius  $\sim 30 \text{ \AA}$ ). Thus, pair distance distribution functions were calculated from the SANS data using the program GNOM (26) according to the equation

$$I(Q) = 4\pi \int_0^{D_{\max}} P(r) \frac{\sin(Qr)}{Qr} dr \quad (2)$$

where  $P(r)$  is related to the probability of two scattering centers (nuclei for SANS) being a distance  $r + dr$  apart and  $D_{\max}$  is the maximum distance between scattering centers within the protein or protein oligomer.  $I(0)$  values were then obtained from the PDDFs through  $I(0) = 4\pi \int_0^{D_{\max}} P(r) dr$ , which has the advantage of utilizing the entire  $Q$  range to determine  $I(0)$ , as opposed to just the low  $Q$  values as in Guinier analysis (27).

The small-angle X-ray scattering data were measured using the X21 beamline at the National Synchrotron Light Source at the Brookhaven National Laboratory (28). The X-ray wavelength was set to  $1.24 \text{ \AA}$  with a pair of Si(111) monochromator crystals. The sample-to-detector distance was calibrated to be 1.69 m using a silver behenate standard. To avoid radiation damage, solutions were continuously passed at a flow rate of  $60 \mu\text{L}/\text{min}$  through a 1 mm glass capillary housed within an aluminum block containing Plexiglas observation windows (28). The net intensities were corrected for the background and solvent scattering, as well as sample transmission, and were put on an absolute scale by comparison with a calibration standard [10 mg/mL BSA (10)].

Infrared spectra were measured with a Genesis II FT-IR spectrometer (Mattson Instruments). Solutions were loaded in a demountable liquid cell equipped with a circulating water jacket ( $T = 20 \text{ }^\circ\text{C}$ ) between a pair of  $\text{CaF}_2$  windows using a  $50 \mu\text{m}$  Teflon spacer. A liquid light guide (Oriel, model 77557) was used to directly illuminate the sample with UV or visible light for 2 h prior to and during data collection, as previously described (9). The sample chamber was continu-

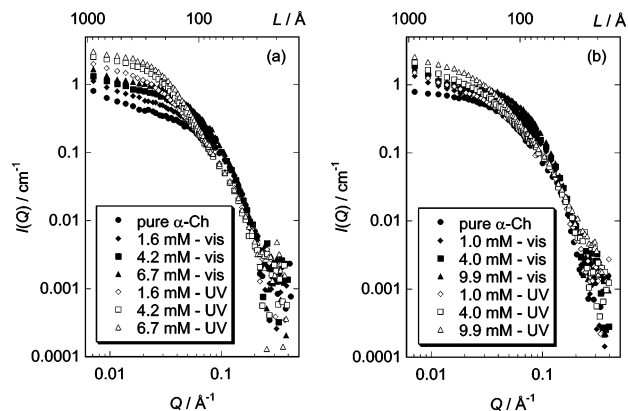


FIGURE 1: SANS data of  $\alpha$ -chymotrypsin/azoTAB solutions as a function of surfactant concentration and light illumination at (a) pH 3.0, 11.6 mg/mL protein, and (b) pH 7.2, 11.4 mg/mL protein.

ously purged with dry air to eliminate the influence of water vapor. For each spectrum, a 500-scan interferogram was collected with a  $2 \text{ cm}^{-1}$  resolution. The relatively sharp surfactant peaks at  $\sim 1600 \text{ cm}^{-1}$  were removed by subtracting the spectra measured for a pure surfactant solution under otherwise identical conditions, resulting in corrected spectra that were flat in the region between 2000 and  $1750 \text{ cm}^{-1}$ . Fourier self-deconvolution (FSD) was applied to spectra to resolve the overlapping bands in the amide I region using a band-narrowing factor  $k = 2.0$  and a full width at half-height of  $12.6 \text{ cm}^{-1}$ . Second derivative spectra were obtained with the Savitsky–Golay function for a third order polynomial, using a 13 data point window. Difference spectra were obtained by subtracting the spectra collecting under visible light from the spectra collecting under UV light illumination. Difference spectra obtained for pure  $\alpha$ -chymotrypsin solutions without surfactant show no significant absorbance changes ( $<1\%$  throughout the amide I region).

Optical microscopy was performed on an Olympus IX71 inverted fluorescence microscope equipped using a  $50\times$  lens (Olympus, model SLCPlanFl) and a U-N41027 CAL CRIM C58158 filter cube (Chroma, model C58158). Images were recorded with a Hamamatsu digital CCD camera (model C4742-95). Aliquots ( $5\text{--}10 \mu\text{L}$ ) of the protein–surfactant solution were deposited onto glass slides and dyed with an equal volume of a  $400 \mu\text{M}$  Congo red aqueous solution.

Transmission electron microscopy was performed on a Philips EM420 TEM operating at 80 kV. A drop of protein solution was placed on a carbon-coated grid for 10 s and then blotted with filter paper, followed by repeating this procedure with a second drop. The grid was then placed in a freshly made 1 wt % uranyl acetate solution for 30 s.

## RESULTS AND DISCUSSION

SANS data for  $\alpha$ -Ch/azoTAB mixtures are shown in Figure 1 as a function of pH, surfactant concentration, and light illumination. AzoTAB undergoes a photoisomerization to the relatively hydrophilic *cis* form when illuminated with 350 nm UV light, which can be reversed back to the relatively hydrophobic *trans* form upon exposure to 434 nm visible light (23). In *inverse space* (e.g., with  $Q$  in units of  $\text{\AA}^{-1}$ ), the transitions responsible for SANS intensity changes

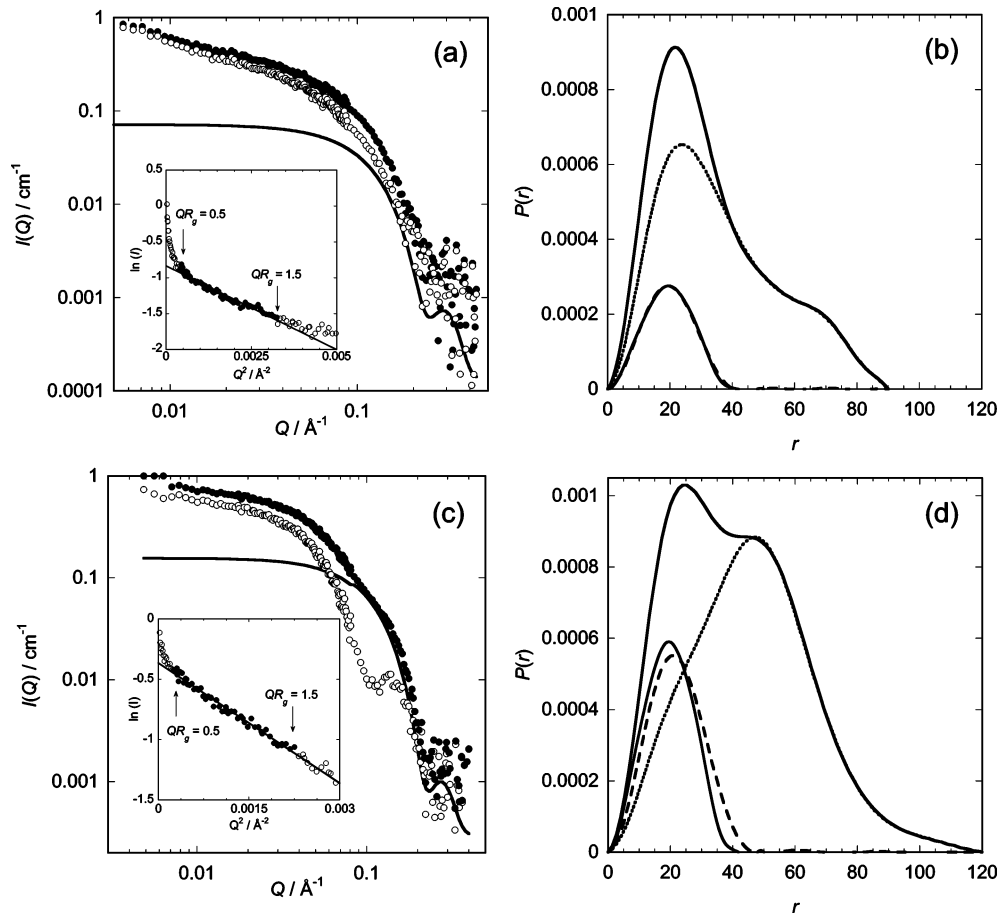


FIGURE 2: SANS data of pure  $\alpha$ -chymotrypsin solutions at (a) pH 3 and (c) pH 7: raw data ( $\bullet$ ), scaled PDB (2CHA) (—), and raw data minus the scaled PDB ( $\circ$ ). Insets show Guinier analysis of the raw data. Also shown are pair distance distribution functions at (b) pH 3.0 and (d) pH 7: raw data (—) and oligomer-only data (dotted). For comparison the raw data minus the oligomer data (dashed) and 2CHA (—) are displayed.

in Figure 1 can be difficult to conceptualize; thus, the *real space* length scale  $L (=2\pi/Q)$  is plotted on the upper  $x$ -axis. The addition of azoTAB causes an increase in scattering at low  $Q$  (i.e.,  $L > 100 \text{ \AA}$ ), suggesting the surfactant induces monomer  $\rightarrow$  oligomer associations. UV light illumination further enhances this effect, with a shift in the scattering curves to lower  $Q$  indicating greater protein aggregation when the surfactant is converted to the *cis* form. Thus, the *trans* isomer appears to be capable of replacing protein–protein interactions with protein–surfactant interactions. Beyond  $Q > 0.2 \text{ \AA}^{-1}$  ( $L < 30 \text{ \AA}$ , or length scales less than the protein diameter) the SANS data converge, suggesting that the individual protein subunits remain relatively intact. However, at high  $Q$  the limiting sensitivity of the SANS data is approached due to weak sample scattering relative to incoherent scattering from the protein ( $0.003 \text{ cm}^{-1}$ ) and solvent ( $0.0004 \text{ cm}^{-1}$  for 99.9%  $\text{D}_2\text{O}$ ).

For associating systems, SANS has two advantageous properties. First, SANS is an *absolute* technique with the weight-average molecular weight ( $M_w$ ) of the sample given directly by  $I(0)$ , the scattering at zero angle (see also Experimental Procedures). Thus, the weight fraction of protein existing as monomer ( $x_1$ ) and  $n$ -mer ( $x_n = 1 - x_1$ ) can be calculated from  $M_w = x_1 M_{w,1} + (1 - x_1) M_{w,n}$ , where  $M_{w,1}$  and  $M_{w,n}$  are the monomer and  $n$ -mer molecular weights, respectively. Second, SANS is *additive* with the scattering for a mixture of monomer (1-mer) and  $n$ -mer species given

by the sum of the contributions from each oligomer  $o$  from 1 to  $n$  (29)

$$I(Q) = n_p \left( \sum_{o=1}^n \frac{N_o}{N} \left| F_o(Q) \right|^2 \right) \bar{S}(Q) \quad (3)$$

where  $n_p = 1/V \sum_{o=1}^n N_o = N/V$  is the total number of particles per volume,  $N_o/N$  is the number fraction of a given type of oligomer,  $F_o(Q)$  is the form factor for that oligomer, and  $\bar{S}(Q)$  is the averaged structure factor related to the partial structure factors  $S_{ij}(Q)$ . Hence for a noninteracting mixture of monomer and a single  $n$ -mer (30), the scattering intensity can be shown to be  $I = \nu_1 I_1 + \nu_n I_n$ , where  $\nu_1$  and  $\nu_n$  are the fractions of protein existing as monomer and  $n$ -mer on a volume basis (not to be confused with the volume fraction in solution,  $\phi = c\bar{v}/1000$ , where  $c$  is the protein concentration in mg/mL units and  $\bar{v}$  is the protein specific volume), while  $I_1$  and  $I_n$  are the scattering from pure monomer and  $n$ -mer, respectively (27). Since  $\nu_i \sim x_i$ , assuming that  $\bar{v}$  is constant independent of oligomeric state, the total scattering intensity is then also given by the linear combination  $I = x_1 I_1 + x_n I_n$  (31). Thus, these two properties of SANS can be utilized to assign the contributions of the overall scattering to the monomer and  $n$ -mer, followed by shape reconstruction to determine the *in vitro* structure of  $\alpha$ -Ch oligomers. In the sections that follow this will first be illustrated for pure  $\alpha$ -Ch

Table 1: Values of Radius of Gyration ( $R_g$ ),  $I(0)$ , Resulting  $n$ -mer ( $n^{\text{eff}}$ ), Fraction of Oligomer ( $x_n$ ), and Radius of Gyration of Oligomer-Only Data ( $R_g^{\text{oligo}}$ ) Determined from Guinier or PDDF Analysis of SANS Data in Figure 1

	pH 3	visible light				UV light		
PDDF	[azoTAB]/mM	0	1.59	4.23	6.70	1.59	4.23	6.70
	$R_g/\text{\AA}$	27.0	34.3	35.4	34.7	52.9	54.1	53.6
	$I(0)/\text{cm}^{-1}$	0.42	0.68	0.97	1.23	1.58	2.34	3.06
	$n^{\text{eff}}$	1.7	2.7	3.8	4.8	6.2	9.2	12.0
	$x_n$	0.66	0.34	0.56	0.77	0.47	0.74	1.0
Guinier	$R_g^{\text{oligo}}/\text{\AA}$	28.9	37.6	37.6	36.0	52.9	53.4	53.6
	$R_g/\text{\AA}$	26.6	32.6	33.6	32.7	57.2	53.7	50.9
	$I(0)/\text{cm}^{-1}$	0.44	0.67	0.94	1.18	1.81	2.46	2.96
	$n^{\text{eff}}$	1.7	2.6	3.7	4.6	7.1	9.7	11.6
	$x_n$	0.71	0.33	0.54	0.73	0.56	0.76	0.94
	$R_g^1/\text{\AA}$	17.4	17.5	17.9	18.1	17.5	17.9	17.5
	$R_g^2/\text{\AA}$	27.5	35.2	35.3	33.5	49.7	50.4	50.1
	pH 7	visible light				UV light		
PDDF	[azoTAB]/mM	0	1.03	4.03	9.92	1.03	4.03	9.92
	$R_g/\text{\AA}$	33.3	30.2	29.2	27.4	44.7	49.5	50.1
	$I(0)/\text{cm}^{-1}$	0.72	0.75	0.90	1.11	1.03	1.42	2.01
	$n^{\text{eff}}$	2.9	3.0	3.6	4.4	4.1	5.7	8.1
	$x_n$	0.38	0.40	0.52	0.69	0.28	0.43	0.64
Guinier	$R_g^{\text{oligo}}/\text{\AA}$	36.0	34.3	32.5	26.6	49.4	49.5	49.8
	$R_g/\text{\AA}$	31.6	33.4	31.5	25.6	48.8	54.1	49.6
	$I(0)/\text{cm}^{-1}$	0.69	0.82	0.95	1.06	1.12	1.57	2.04
	$n^{\text{eff}}$	2.8	3.3	3.8	4.2	4.5	6.3	8.2
	$x_n$	0.36	0.45	0.56	0.65	0.32	0.48	0.65
	$R_g^1/\text{\AA}$	17.0	18.0	18.2	17.8	17.2	17.1	17.5
	$R_g^2/\text{\AA}$	36.4	34.7	32.9	25.9	44.1	45.3	45.6

and then extended to solutions containing azoTAB to demonstrate photocontrolled  $\alpha$ -Ch association.

**Pure Protein Solutions.**  $\alpha$ -Ch is well-known to self-associate through either a monomer–dimer (pH 3) or monomer–hexamer (pH 7) equilibrium at low ionic strength (32–34), with a reduction in the overall positive charge of the protein ( $pI = 9.1$ ) with increased pH generally allowing for greater association. The SANS data for pure  $\alpha$ -Ch solutions shown in Figure 1, measured at conditions where self-association is expected to be prevalent ( $\sim 10$  mg/mL protein), are replotted in Figure 2. The raw data are largely featureless due to the presence of both monomer and oligomer in solution, complicating quantitative analysis of the self-association process. To deconvolute the scattering data, the weight-average molecular weight ( $M_w$ ) of each sample was calculated from the scattering at zero angle, reported as the effective oligomer size ( $n^{\text{eff}} = M_w/M_i$ ) in Table 1.  $I(0)$  values determined from both Guinier plots (25) using  $I(Q) = I(0) \exp(-Q^2 R_g^2/3)$ , technically valid for  $QR_g < 1.3$  as discussed below, where  $R_g$  is the radius of gyration (Figure 2a,c, insets), and from the entire  $Q$  range using pair distance distribution functions (PDDFs) in Figure 2b,d are generally consistent. Note that the steep upturn in the Guinier plots at  $Q < 0.01 \text{ \AA}^{-1}$  ( $L > 600 \text{ \AA}$ ) could be due to the presence of a small amount of higher order aggregates, which due to the characteristic  $Q^{-4}$  decay would not be expected to influence the data analyses employed below.

From the  $M_w$  value determined at each pH, the weight fractions of monomer and  $n$ -mer were calculated. The portion of the scattering resulting from free monomers, estimated from the monomer PDB file 2CHA using the program CRYSON (35) and scaled with a monomer concentration of  $x_1 c$  as shown in Figure 2a,c, was then subtracted from the

overall scattering to give the oligomer-only SANS data. This procedure presumes that the structure of the monomer in vitro is well represented by the native X-ray crystallographic structure, shown to be true for a range of soluble proteins (12, 36, 37). Compared to the featureless raw data, the oligomer scattering curve at pH 7 displays a prominent peak at  $Q = 0.14 \text{ \AA}^{-1}$ , translating in real space to  $L \sim 45 \text{ \AA}$ , also detected as a peak in the corresponding PDDF curve. This dimension corresponds to a highly probable distance within the protein oligomer, namely, the separation distance between monomers. Peaks in this  $Q$  range signify well-ordered oligomer conformations and are often used as qualitative tests for oligomer formation (38), lending confidence in the deconvolution procedure. Oligomer peaks become more pronounced with increasing  $n$ -mer size; thus, it is not surprising that the dimer data at pH 3 do not display this peak.

Following deconvolution, shape reconstructions of the oligomer-only data were performed, conceptually similar to previous studies used to determine the in vitro structures of partially folded BSA (9, 10) and lysozyme (11). The GA\_STRUCT program begins with chains of randomly oriented “scattering centers” (i.e., atomic nuclei for SANS), with a genetic algorithm consisting of matings, mutations, and extinctions used to update the shape (15). Despite this general procedure, the dimer (pH 3) and hexamer (pH 7) structures indeed contain  $n$  subunits for each  $n$ -mer, as shown in Figure 3. Interestingly, the SANS-based in vitro dimer is not consistent with the “face-to-face” (active site-to-active site) crystal packing of  $\alpha$ -chymotrypsin and is instead better represented by the “back-to-side” packing of chymotrypsinogen (2CGA; note that  $\alpha$ -Ch results from the removal of two dipeptides at positions 14–15 and 147–148 in chymotrypsinogen). For example, the maximum dimension of 6CHA  $\sim 70 \text{ \AA}$ , while the PDDF in Figure 2b gives a  $D_{\text{max}}$  of  $\sim 90 \text{ \AA}$  compared to  $\sim 85 \text{ \AA}$  for 2CGA. This serves to highlight the influence that crystal-packing constraints can have on molecular orientations, a significant advantage of SANS in the study of protein aggregates, and could explain why the role of the active site in  $\alpha$ -Ch association remains unsolved in the literature with different techniques yielding conflicting results (32).

Shape reconstruction of the pH 7 data reveals the compact, “W-shaped” hexamer shown in Figure 3b. The average distance between nearest-neighbor subunits is  $43 \pm 5 \text{ \AA}$ , in agreement with the  $0.14 \text{ \AA}^{-1}$  peak in Figure 2c, while the orientation angle between the centers of mass of three successive subunits is estimated as  $70 \pm 10^\circ$  from the 3D shape reconstructions. The consistency of these values suggests that specific intermolecular interactions are responsible for hexamer formation in solution, resulting in the twisted arrangement of the subunits. Interestingly, the ribbon diagram of a hypothetical hexamer constructed by continuing the relative orientation of the two macromolecules in 2CGA (with alternate proteins color-coded blue and green) exhibits a similar twisted orientation, with all but the final protein in nearly identical locations. In contrast, the face-to-face arrangement of 6CHA would not support higher order association, as opposed to the “heterologous association” apparently observed in Figure 3a (31). Also shown in the inset of Figure 3 is the consensus envelope obtained by docking and averaging ten independent fits of

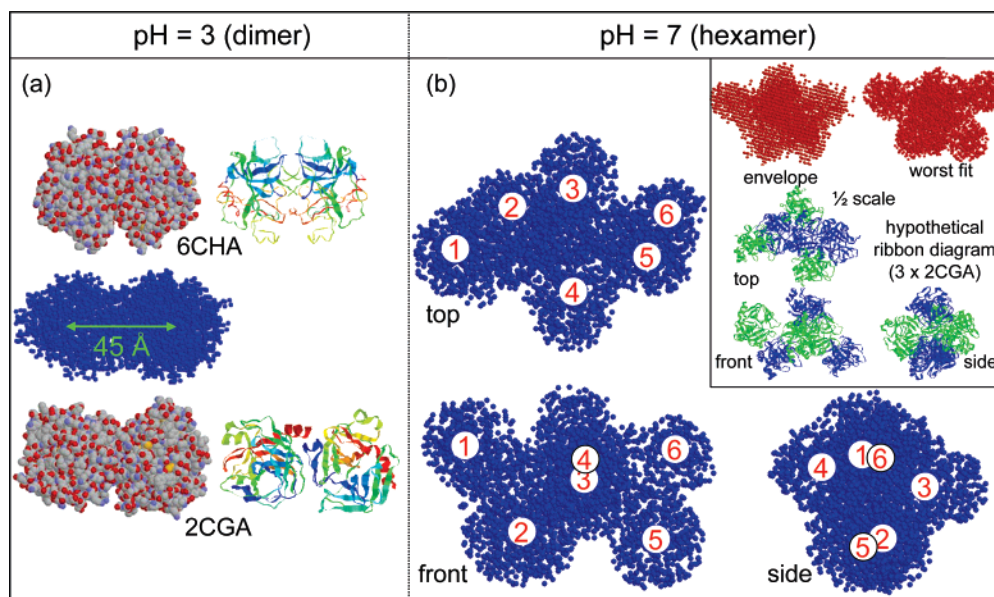


FIGURE 3: Shape reconstructions of the oligomer-only SANS data for pure  $\alpha$ -chymotrypsin at (a) pH 3 and (b) pH 7 (in blue) compared to the X-ray crystallographic structures of the  $\alpha$ -chymotrypsin dimer (PDB code 6CHA) and chymotrypsinogen-A dimer (PDB code 2CGA) at pH 3. The insert shows a hypothetical hexamer built from three 2CGA subunits (alternating monomers shown in blue and green) along with the consensus envelope and worst fit (shown in red).

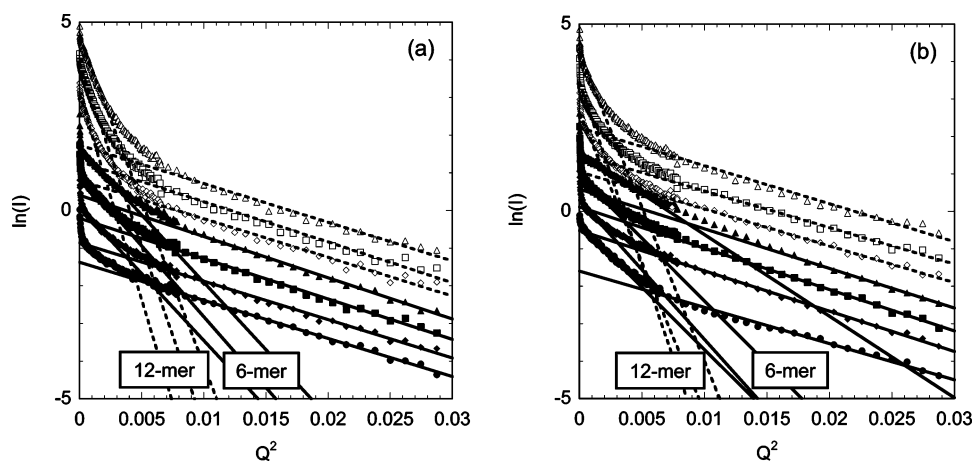


FIGURE 4: Guinier analysis of the raw SANS data. (a) pH 3: pure  $\alpha$ -Ch ( $\bullet$ ), 1.59 mM azoTAB visible ( $\blacklozenge$ ) and UV ( $\diamond$ ), 4.23 mM visible ( $\blacksquare$ ) and UV ( $\square$ ), and 6.70 mM visible ( $\blacktriangle$ ) and UV ( $\triangle$ ). (b) pH 7: pure  $\alpha$ -Ch ( $\bullet$ ), 1.03 mM visible ( $\blacklozenge$ ) and UV ( $\diamond$ ), 4.03 mM visible ( $\blacksquare$ ) and UV ( $\square$ ), and 9.92 mM visible ( $\blacktriangle$ ) and UV ( $\triangle$ ). Data sets are successively offset by 0.5 logarithmic units.

the GA\_STRUCT program, along with the run that statistically produced the worst fit to the data. Both of these structures agree with the W-shaped hexamer conformation, demonstrating that the coupled deconvolution/shape-reconstruction technique can be applied to protein oligomers in solution. Non-native protein conformations such as partially folded or associated states challenge existing crystallographic and NMR methods. However, as demonstrated in Figure 3 and in recent studies of photocontrolled protein folding (10, 11), SANS can provide valuable information on these important yet understudied class of structures.

*$\alpha$ -Chymotrypsin/azoTAB Solutions.* As discussed above, qualitative assessment of the SANS data in Figure 1 indicates enhanced  $\alpha$ -Ch association with either increased surfactant concentration or upon converting azoTAB from the *trans* to the *cis* form with UV light illumination. To quantitatively investigate this phenomenon, Guinier plots of the SANS data for  $\alpha$ -Ch/azoTAB solutions were generated, as shown in Figure 4. Two unique slopes can be detected at each condition, the first in the region of  $Q^2 < 0.002 \text{ \AA}^{-2}$

corresponding to the  $z$ -average radius of gyration of the mixture and the second at  $Q^2 \sim 0.01\text{--}0.03 \text{ \AA}^{-2}$  with  $R_g^1$  values ranging from 17.0 to 18.2  $\text{\AA}$ , as shown in Table 1. These latter values are consistent with the  $R_g$  of monomeric  $\alpha$ -Ch in the literature of 16.9  $\text{\AA}$  (39), thus indicating a monomer/ $n$ -mer equilibrium (40, 41) similar to the monomer-oligomer equilibrium observed during the early stages of fibril formation of  $A\beta$  proteins (1, 8). The 7% increase in  $R_g^1$  with the addition of azoTAB in Table 1 indicates that a slight unfolding of the protein could be the cause of increased association, consistent with the general observation that partially unfolded protein conformations can lead to amyloid fibril formation (1). For example, intermediate trifluoroethanol concentrations where non-native conformations are stabilized through still favorable hydrogen bonding between peptides (42) can induce amyloid formation in a variety of proteins including  $\alpha$ -Ch (5). The amphiphilic nature of azoTAB has also been shown to stabilize partially unfolded intermediates in proteins such as BSA and lysozyme (10, 11). It should be pointed out, however, that the Guinier region

is strictly valid only for  $QR_g < 1.3$ , while the above fits span  $Q^2 = 0.01\text{--}0.03 \text{ \AA}^{-2}$  ( $QR_g = 1.7\text{--}3$ ). Replacing  $[3j_1 - (QR_g)/QR_g]^2$  with the approximate expression  $\exp(-Q^2 R_g^2/3)$ , as suggested by Guinier (25), results in deviations on the order of 10% over this  $Q$  range.

From the fits in the low  $Q$  region of Figure 4, the  $R_g$  values are approximately constant at a given pH and light condition, suggesting that the oligomer size is primarily determined by the state of the surfactant.  $I(0)$  values determined from either the Guinier plots in Figure 4 for  $Q^2 < 0.002 \text{ \AA}^{-2}$  or PDDFs of the overall data (not shown) are displayed in Table 1, along with the effective oligomer size ( $n^{\text{eff}}$ ). Together, these values suggest monomer–hexamer equilibrium for the visible light data and a monomer–dodecamer equilibrium under UV light; however, unlike pure  $\alpha$ -chymotrypsin the oligomer size is not known a priori. Nevertheless, additional evidence will be presented below to support this type of protein self-association. In truth, these  $n$ -mer assignments are a result of a comprehensive iterative procedure whereby the number of protein subunits observed from shape reconstruction of the raw data (monomer plus oligomer) was used to provide initial estimates of  $n$ . However, since fitting the overall data would return the  $z$ -averaged shape of the protein (43), which is heavily weighted toward the oligomer conformation, 6 and 12 subunits could be consistently detected even from the raw data (see below). Furthermore, for the UV data, the choice of  $n = 12$  was particularly clear given that both the SANS and SAXS data (Figure 8 below) appear to converge to an  $n^{\text{eff}}$  value of 12 with increasing surfactant concentration.

It is important to note that the measured increases in  $I(0)$  cannot simply be the result of surfactant binding alone. First, by comparing the surfactant to protein molar ratios, only between 2.5 and 25 surfactant molecules could possibly be bound per protein over the range of surfactant concentrations studied assuming complete surfactant binding. This would equate to at most an increase in the effective molecular weight of between 4% and 40%, much smaller than the 12-fold increase observed during dodecamer formation. Thus, it is immediately clear that the primary role of the surfactant is to induce protein aggregation. Nevertheless, control experiments were performed at the protein contrast-matching point (60/40  $\text{H}_2\text{O}/\text{D}_2\text{O}$ ), thereby rendering the protein “invisible” to the neutron beam. The SANS spectrum obtained from this contrast-matched sample (not shown) was within the experimental error, indicating minimal to no scattering from azoTAB. Hence, the increases observed in this report can be conclusively attributed to protein aggregation.

From the resulting  $n$ -mer assignments above, the monomer weight fraction was calculated, indicating that the monomer–oligomer equilibrium shifts toward  $n$ -mer formation with increasing surfactant concentration, a likely result of increased partial unfolding as mentioned above. To gain further insight in the oligomer structures, the SANS data were deconvoluted as above to obtain the portion of the scattering due only to the  $n$ -mers. As shown in Figure 5, the  $x_r$ -scaled oligomer scattering data are largely consistent for a given pH and light conditions, suggesting a sound deconvolution procedure. Some subtle changes are observed with increasing surfactant concentration within a given data set, particularly in the high  $Q$  region representing fine structural detail.

Specifically, the peak observed at  $Q \sim 0.2 \text{ \AA}^{-2}$ , similar to the deconvoluted hexamer of pure  $\alpha$ -Ch at pH 7, becomes “washed out” with increasing azoTAB concentration, suggesting that the oligomers become more disordered with increased fluctuations in the protein subunit positions. Using Guinier plots (not shown) to calculate of the radius of gyration from each oligomer-only scattering profile gives the values of  $R_g^n$  reported in Table 1.

PDDFs calculated from the oligomer-only data display a similar degree of homogeneity at each condition with increasing surfactant, as shown in Figure 5a,b. Interestingly, independent of oligomer type (hexamer or dodecamer)  $R_g^n \propto (M_w)^{0.42 \pm 0.03}$  compared to the monomer radius of gyration, where  $M_w$  is the molecular weight of the oligomer. A similar scaling exponent (0.45) has been reported for self-associating insulin, with values intermediate between those expected for spheres ( $1/3$ ) or Gaussian coils ( $1/2$ ), suggesting relatively open oligomer structures (30).

Comparing the visible light (hexamer) PDDFs to Figure 2d for the pure hexamer reveals a shift in the PDDF peak to lower  $r$  values. This suggests a potential unraveling of the tightly packed W-shaped hexamer with the most probable dimension being reduced to distances within the protein subunits (e.g., the protein radius) as opposed to distances between the subunits. However, note that  $D_{\text{max}}$  of the hexamer remains at  $\sim 120 \text{ \AA}$  as in Figure 2d; thus, only partial unraveling can be occurring, largely retaining the twisted hexamer conformation. For example, a linear  $n$ -mer formed from a protein with a radius of  $20 \text{ \AA}$  would give peaks at  $20, 40, \dots, (n-1)40 \text{ \AA}$ . For the dodecamer structures the most probable dimension returns to  $40\text{--}50 \text{ \AA}$ , while  $D_{\text{max}}$  undergoes a modest increase to  $\sim 160 \text{ \AA}$ ; hence, longitudinal extension of hexamers to form dodecamers does not appear to be an appropriate mechanism. Shoulders can also be detected in the PDDF curves at  $\sim 80, 100, \text{ and } 120 \text{ \AA}$  corresponding to distances between higher order neighbors, suggesting regular, as opposed to random, oligomer conformations. Guinier analyses of the oligomer-only data (not shown) give radii of gyration of the  $n$ -mers ( $R_g^n$ ) consistent with the PDDF analysis as displayed in Table 1, again largely independent of surfactant concentration across a given data set. Taken together, this evidence suggests that converting azoTAB to the *cis* form with UV light causes hexamers to laterally (as opposed to longitudinally) associate into dodecamers.

To obtain a better understanding of the oligomer conformations, shape reconstruction was applied to the deconvoluted SANS data, as shown in Figure 6. In all cases the shape-reconstruction algorithm returned conformations containing either 6 or 12 subdomains, despite the fact that the program begins with a random arrangement of scattering centers. This fact further confirms the choice of hexamers and dodecamers, as well as the overall deconvolution procedure. The shape-reconstructed hexamers indeed support the notion above of an unraveling of the W-shaped hexamer, as the hexamers now have extended, corkscrew-like appearances. Upon UV illumination and conversion of the surfactant to the *cis* form, hexamers are converted into the rope-like dodecamers, suggesting that dodecamer formation results from lateral association of two hexamers. This is illustrated by the bead-model structures accompanying each  $90^\circ$  rotation view of

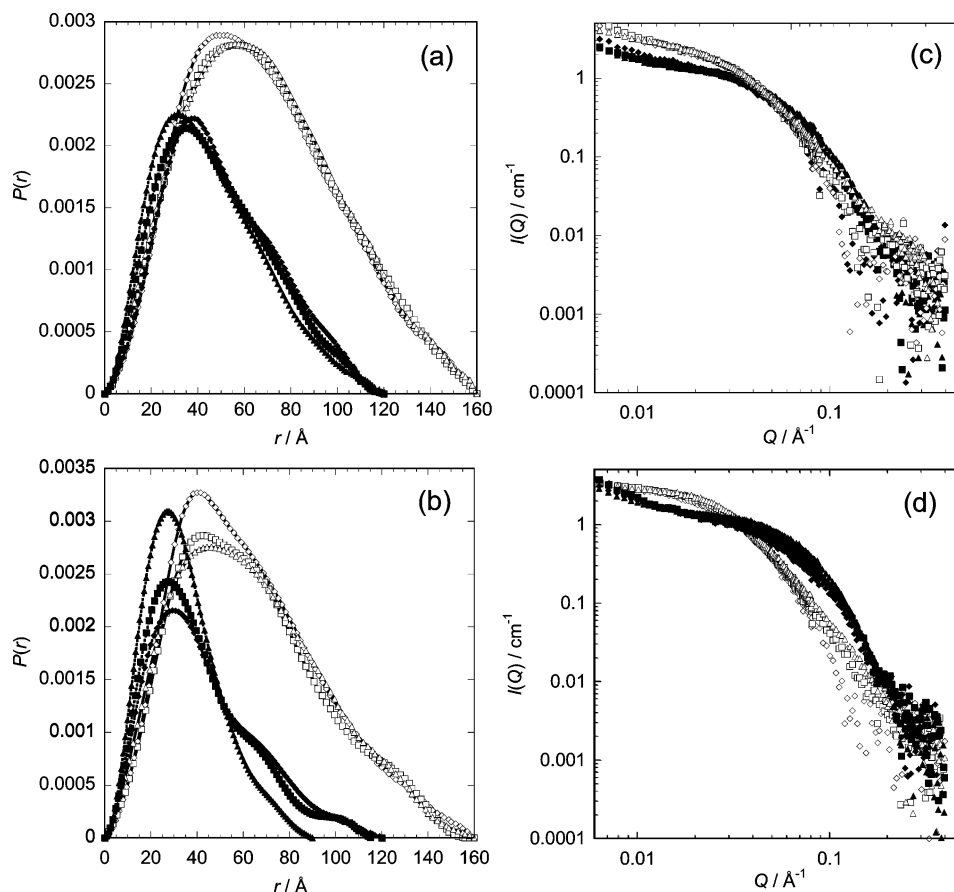


FIGURE 5: Pair distance distribution functions of the oligomer-only data scaled by the respective oligomer weight fractions. (a) pH 3: 1.59 mM azoTAB visible ( $\blacklozenge$ ) and UV ( $\diamond$ ), 4.23 mM visible ( $\blacksquare$ ) and UV ( $\square$ ), and 6.70 mM visible ( $\blacktriangle$ ) and UV ( $\triangle$ ). (b) pH 7: pure  $\alpha$ -Ch ( $\bullet$ ), 1.03 mM visible ( $\blacklozenge$ ) and UV ( $\diamond$ ), 4.03 mM visible ( $\blacksquare$ ) and UV ( $\square$ ), and 9.92 mM visible ( $\blacktriangle$ ) and UV ( $\triangle$ ). Also shown are the SANS scattering curves of the oligomer-only data. (c) pH 3: 1.59 mM azoTAB visible ( $\blacklozenge$ ) and UV ( $\diamond$ ), 4.23 mM visible ( $\blacksquare$ ) and UV ( $\square$ ), and 6.70 mM visible ( $\blacktriangle$ ) and UV ( $\triangle$ ). (d) pH 7: pure  $\alpha$ -Ch ( $\bullet$ ), 1.03 mM visible ( $\blacklozenge$ ) and UV ( $\diamond$ ), 4.03 mM visible ( $\blacksquare$ ) and UV ( $\square$ ), and 9.92 mM visible ( $\blacktriangle$ ) and UV ( $\triangle$ ).

the oligomers, used to guide the eye as to the relative positions of each protein subunit. The observed  $n$ -mer structures are found to be reasonably consistent across the range of pH and surfactant concentration conditions, again pointing to the global consistency of the deconvolution procedure.

**Photoinduced  $\alpha$ -Chymotrypsin Oligomers Are Amyloid Precursors.** The lateral association of hexamers into dodecamers is consistent with the eventual rope-like conformation commonly observed in many amyloid fibrils, indicating that SANS may be reporting on the mechanism of formation of key prefibrillar intermediates in the amyloid cascade. To investigate whether the oligomer structures in Figure 6 are true prefibrillar intermediates, several classic amyloid tests were performed on azoTAB/ $\alpha$ -Ch mixtures. FT-IR spectra of pure  $\alpha$ -Ch and  $\alpha$ -Ch in the presence of azoTAB under both visible and UV light are shown in Figure 7a,b. Two aggregation processes can be triggered in the  $\alpha$ -Ch/azoTAB system: the first upon the addition of *trans* azoTAB to pure  $\alpha$ -Ch (dimers  $\rightarrow$  hexamers at pH 3) and the second upon exposure of the  $\alpha$ -Ch/azoTAB system to UV light (hexamers  $\rightarrow$  dodecamers). As seen in the FT-IR spectra, both of these association processes give rise to an increase in peaks at 1612 and 1685  $\text{cm}^{-1}$ , characteristic of *intermolecular*  $\beta$ -sheet formation (44–46), at the expense of the peak at 1637  $\text{cm}^{-1}$  commonly assigned to *intramolecular*  $\beta$ -sheets (47, 48). Zurdo et al. observe bands at 1612 and 1685  $\text{cm}^{-1}$  in SH3

domain protofibril intermediates that eventually mature into fully developed amyloid fibrils (45), suggesting that the oligomers observed in Figure 6 are indeed precursors to amyloid structures.

The photomicrographs shown in Figure 7c,d further support this conclusion. Congo red staining of a  $\alpha$ -Ch/azoTAB solution aged for 5 days results in characteristic Congo red fluorescence as well as “apple green” birefringence, respectively. Congo red preferentially stains amyloid structures due to the planar structure of the dye favoring incorporation into the  $\beta$ -sheet structure of amyloids (49–51). These images were also accompanied by Maltese-cross patterns under cross-polarizers (not shown) indicative of spherulites formed by the aligning of fibrils in a radial pattern (52).

TEM images in Figure 7 further demonstrate the formation of fibrillar structures. Panels e and f of Figure 7 were obtained 2 weeks after preparing a fresh  $\alpha$ -Ch/azoTAB solution, while Figure 7g was obtained from an original SANS solution (pH 3, [azoTAB] = 4.2 mM) approximately 1 year after collecting the SANS spectra. The fibrils shown in Figure 7e–g possess clear amyloid characteristics: they are long, unbranched, and appear to be twisted, with diameters of ca. 10 nm. Combined, these tests confirm that the structures obtained from the SANS measurements in Figure 6 are indeed preamyloid oligomer intermediates.

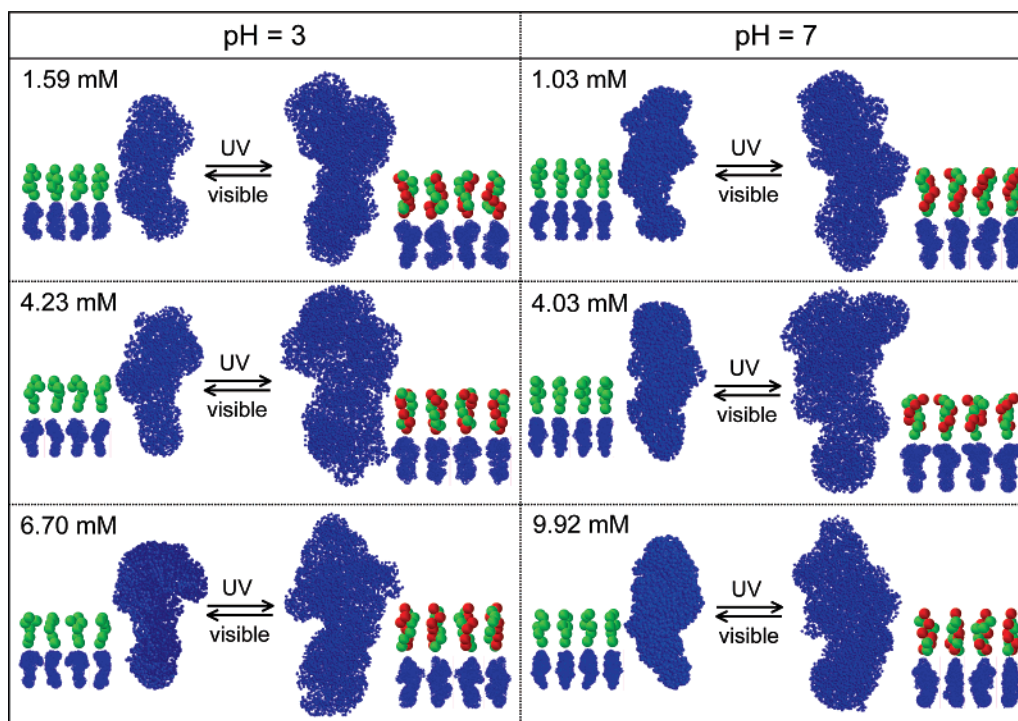


FIGURE 6: Shape reconstructions of the oligomer-only SANS data at pH 3 and pH 7 as a function of azoTAB concentration and light illumination. Inserts show four views of the shape reconstructions rotated at  $90^\circ$ , along with low-resolution globular models designed to mimic the twisted conformations detected in the structures (PDB files available upon request).

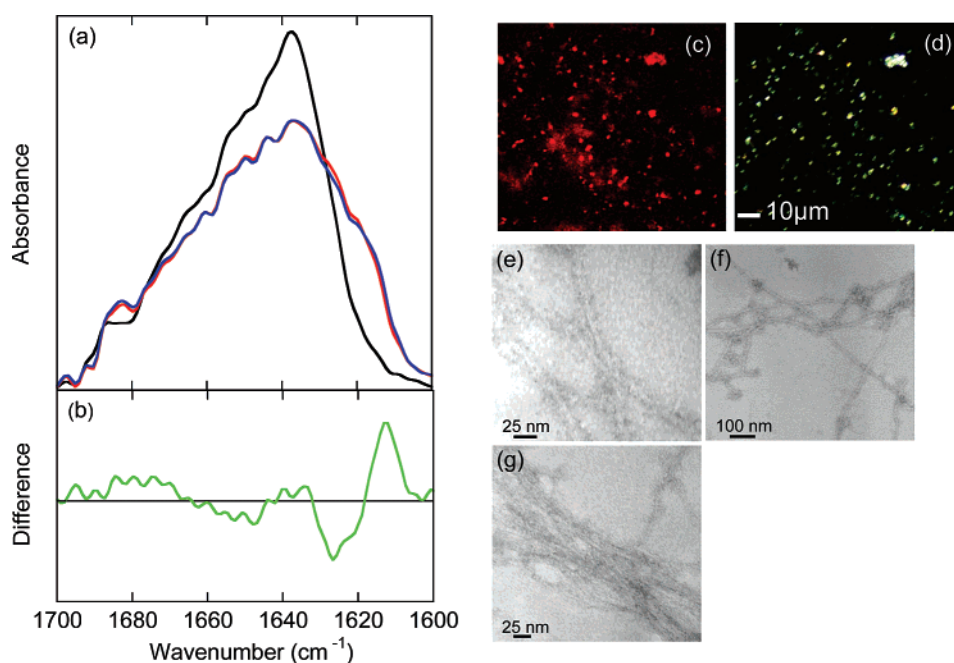


FIGURE 7: (a) FT-IR absorbance spectra at pH 3 for pure  $\alpha$ -Ch (black line) and mixtures of  $\alpha$ -Ch with 9.04 mM azoTAB under visible light (red line) and UV light (blue line). [ $\alpha$ -Ch] = 11.6 mg/mL. (b) FT-IR difference spectra (UV - visible) demonstrating the effect of light illumination. Also shown are Congo red fluorescence (c) and apple green birefringence (d) obtained under cross-polarizers, as well as TEM images of a fresh solution (e, f) (pH 3, [azoTAB] = 4.95 mM) and an original SANS solution (g) (pH 3, [azoTAB] = 4.23 mM) after an elapsed time of approximately 1 year.

**Photocontrol of Protein Association.** To investigate the photocontrol of protein association, small-angle X-ray scattering (SAXS) data were collected for mixtures of chymotrypsinogen-A and azoTAB at pH 3, as shown in Figure 8. Chymotrypsinogen is the zymogen of  $\alpha$ -chymotrypsin, activated by the removal of two dipeptides at positions Ser14-Arg15 and Thr147-Asn148 leading to the formation of the active site (53). Despite this structural similarity, however,

chymotrypsinogen does not generally associate in solution unlike in the case of  $\alpha$ -chymotrypsin (54, 55).

This phenomenon is supported by the visible light SAXS data in Figure 8a, where a clear intermolecular interaction peak is observed in contrast to Figure 1, consistent with increasing electrostatic repulsion between chymotrypsinogen monomers as the cationic surfactant binds to the positively charged protein. A Guinier plot of the pure protein SAXS

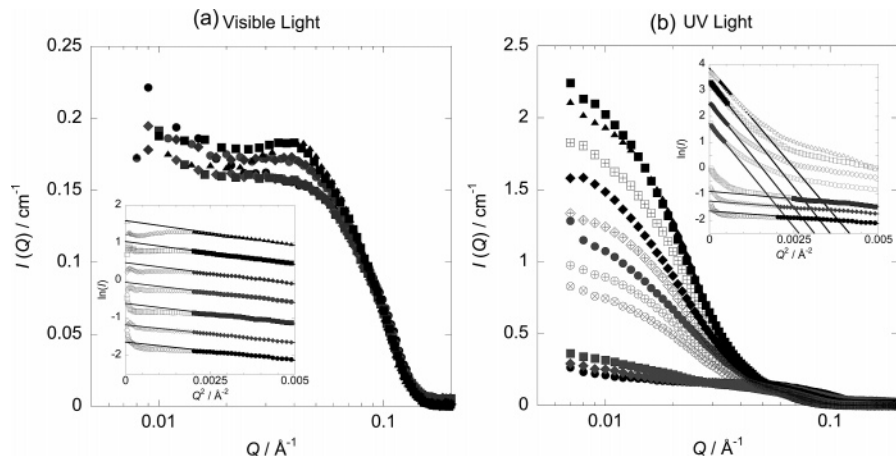


FIGURE 8: SAXS data of chymotrypsinogen-A/azoTAB solutions as a function of surfactant concentration and light illumination at pH 2.7 and 10.0 mg/mL protein under (a) visible light and (b) UV light. Pure  $\alpha$ -Ch ( $\bullet$ ), 2.5 mM azoTAB (gray  $\blacklozenge$ ), 5 mM (gray  $\blacksquare$ ), 10 mM (gray  $\bullet$ ), 14 mM ( $\blacklozenge$ ), 19 mM ( $\blacksquare$ ), and 24 mM ( $\blacktriangle$ ). Also shown are the effects of reillumination with visible light on UV-adapted samples at various exposure times: 19 mM, 1 h (+ in box), 14 mM, 1 h (+ in tilted box), 10 mM, 1 h (+ in circle), and 2 h ( $\times$  in circle). Insets show Guinier fits with successive data sets offset by 0.5 logarithmic units.

Table 2: Values of Radius of Gyration ( $R_g$ ),  $I(0)$ , and Resulting  $n$ -mer ( $n^{\text{eff}}$ ) Determined from Guinier Analysis of the SAXS Data in Figure 8

	[azoTAB]/mM	$R_g/\text{\AA}$	$I(0)/\text{cm}^{-1}$	$n^{\text{eff}}$
visible	0	17.1	0.194	
	2.5	16.9	0.186	
	5.0	18.1	0.200	
	10.0	18.1	0.213	
	14.0	18.5	0.218	
	19.0	19.1	0.231	
UV	24.0	19.7	0.245	
	2.5	17.1	0.172	
	5.0	18.6	0.152	
	10.0	69.2	1.25	6.5
	14.0	69.8	1.73	9.0
	19.0	69.6	2.38	12.4
	24.0	67.9	2.32	12.1

data (Figure 8 inset) gives  $R_g = 17.1 \text{ \AA}$ , similar to the SAXS-derived  $R_g$  value from the literature of  $17.6 \text{ \AA}$  (39). With increasing surfactant concentration,  $R_g$  increases modestly up to 10 mM azoTAB under visible light, eventually increasing to  $19.7 \text{ \AA}$  at 24 mM azoTAB (Table 2). The enhanced negative deviations from the Guinier behavior at low  $Q$  with increasing surfactant concentration are a result of increasing intermolecular interactions.

Under UV light illumination, however, the situation is markedly different, with large increases in the SAXS data observed at low  $Q$  (note that the y-axes of panels a and b of Figure 8 differ by an order of magnitude), particularly at 10 mM azoTAB and beyond, coincidentally the surfactant concentration where the onset of chymotrypsinogen unfolding was observed under visible light. The Guinier plots under UV light also reveal the development of an additional larger species with increasing surfactant concentration, detected by the appearance of a steep slope at low  $Q$ .  $I(0)$  values for samples under visible light [ $\sim 0.2$ – $0.25 \text{ cm}^{-1}$ ; see Table 2, where the SAXS data have been put on an absolute scale by comparing to a calibration standard of 10 mg/mL BSA ( $I(0) = 0.24 \text{ cm}^{-1}$ ), again indicating that chymotrypsinogen association does not occur under visible light. Under UV light a 12-fold increase in  $I(0)$  is observed at 19 and 24 mM azoTAB relative to the monomer data, suggesting that the

association equilibrium is pushed entirely toward dodecamers, providing independent confirmation of the  $\alpha$ -chymotrypsin data.

Partial reversibility of protein self-association is shown in Figure 8b, where SAXS spectra were collected for UV-equilibrated samples following reexposure to 434 nm visible light. The low  $Q$  scattering decreases as a function of visible light exposure time, with apparently several hours required for complete visible light induced dissociation (beyond the limit of the allocated SAXS beam time). However, it should be pointed out that this dissociation process is not limited by the *cis*  $\rightarrow$  *trans* isomerization kinetics, which occurs within minutes (23). Protein association and dissociation can generally occur on time scales ranging from seconds up to hours or even several days (56, 57). Thus, the SAXS data demonstrate the possibility of photoreversible control of protein oligomerization.

#### ACKNOWLEDGMENT

We acknowledge the support of the National Institute of Standards and Technology, U.S. Department of Commerce, in providing the neutron research facilities used in this work. Special thanks are owed to Paul Butler and Boualem Hammouda for helpful discussions. Use of the National Synchrotron Light Source, Brookhaven National Laboratory, was supported by the U.S. Department of Energy, Office of Science, Office of Basic Energy Sciences, under Contract DE-AC02-98CH10886. We thank W. T. Heller for graciously supplying the GA\_STRUCT program.

#### REFERENCES

- Chiti, F., and Dobson, C. M. (2006) Protein misfolding, functional amyloid, and human disease, *Annu. Rev. Biochem.* 75, 333–366.
- Sambashivan, S., Liu, Y., Sawaya, M. R., Gingery, M., and Eisenberg, D. (2005) Amyloid-like fibrils of ribonuclease A with three-dimensional domain-swapped and native-like structure, *Nature (London)* 437, 266–269.
- Booth, D. R., Sunde, M., Bellotti, V., Robinson, C. V., Hutchinson, W. L., Fraser, P. E., Hawkins, P. N., Dobson, C. M., Radford, S. E., Blake, C. C. F., and Pepys, M. B. (1997) Instability, unfolding and aggregation of human lysozyme variants underlying amyloid fibrillogenesis, *Nature* 385, 787–793.
- Brange, J., Andersen, L., Laursen, E. D., Meyn, G., and Rasmussen, E. (1997) Toward understanding insulin fibrillation, *J. Pharm. Sci.* 86, 517–525.

5. Pallares, I., Vendrell, J., Aviles, F. X., and Ventura, S. (2004) Amyloid fibril formation by a partially structured intermediate state of  $\alpha$ -chymotrypsin, *J. Mol. Biol.* **342**, 321–331.
6. Klein, W. L., Stine, W. B., and Teplow, D. B. (2004) Small assemblies of unmodified amyloid  $\beta$ -protein are the proximate neurotoxin in Alzheimer's disease, *Neurobiol. Aging* **25**, 569–580.
7. Kirkitadze, M. D., Bitan, G., and Teplow, D. B. (2002) Paradigm shifts in Alzheimer's disease and other neurodegenerative disorders: the emerging role of oligomeric assemblies, *J. Neurosci. Res.* **69**, 567–577.
8. Yong, W., Lomakin, A., Kirkitadze, M. D., Teplow, D. B., Chen, S.-H., and Benedek, G. B. (2002) Structure determination of micelle-like intermediates in amyloid  $\beta$ -protein fibril assembly by using small angle neutron scattering, *Proc. Natl. Acad. Sci. U.S.A.* **99**, 150–154.
9. Wang, S., and Lee, C. T., Jr. (2006) Protein secondary structure controlled with light and photoresponsive surfactants, *J. Phys. Chem. B* **110**, 16117–16123.
10. Lee, C. T., Jr., Smith, K. A., and Hatton, T. A. (2005) Photocontrol of protein folding: the interaction of photosensitive surfactants with bovine serum albumin, *Biochemistry* **44**, 524–536.
11. Hamill, A., Wang, S.-C., and Lee, C. T., Jr. (2005) Probing lysozyme conformation with light reveals a new folding intermediate, *Biochemistry* **44**, 15139–15149.
12. Timchenko, A. A., Ptitsyn, O. B., Dolgikh, D. A., and Fedorov, B. A. (1978) The structure of ribonuclease in solution does not differ from its crystalline structure, *FEBS Lett.* **88**, 105–108.
13. Chen, S. H., and Teixeira, J. (1986) Structure and fractal dimension of protein-detergent complexes, *Phys. Rev. Lett.* **57**, 2583–2586.
14. Svergun, D. I., Petoukhov, M. V., and Koch, M. H. J. (2001) Determination of domain structure of proteins from X-ray solution scattering, *Biophys. J.* **80**, 2946–2953.
15. Heller, W. T., Krueger, J. K., and Trehwella, J. (2003) Further insights into calmodulin-myosin light chain kinase interaction from solution scattering and shape restoration, *Biochemistry* **42**, 10579–10588.
16. Marone, P. A., Thiyagarajan, P., Wagner, A. M., and Tiede, D. M. (1998) The association state of a detergent-solubilized membrane protein measured during crystal nucleation and growth by small-angle neutron scattering, *J. Cryst. Growth* **191**, 811–819.
17. Hunt, J. F., McCrea, P. D., Zaccai, G., and Engelman, D. M. (1997) Assessment of the aggregation state of integral membrane proteins in reconstituted phospholipid vesicles using small angle neutron scattering, *J. Mol. Biol.* **273**, 1004–1019.
18. Chiti, F., Taddei, N., Bucciantini, M., White, P., Ramponi, G., and Dobson, C. M. (2000) Mutational analysis of the propensity for amyloid formation by a globular protein, *EMBO J.* **19**, 1441–1449.
19. Srisailam, S., Thallampuranam, K., Krishnaswamy, S., Rajalingam, D., Kathir Karuppanan, M., Sheu, H.-S., Jan, F.-J., Chao, P.-C., and Yu, C. (2003) Amyloid-like fibril formation in an all beta-barrel protein. Partially structured intermediate state(s) is a precursor for fibril formation, *J. Biol. Chem.* **278**, 17701–17709.
20. Lee, C. T., Jr., Smith, K. A., and Hatton, T. A. (2004) Photo-reversible viscosity changes and gelation in mixtures of hydrophobically-modified polyelectrolytes and photosensitive surfactants, *Macromolecules* **37**, 5397–5405.
21. Hayashita, T., Kurosawas, T., Miyata, T., Tanaka, K., and Igawa, M. (1994) Effect of structural variation within cationic azo-surfactant upon photoresponsive function in aqueous solution, *Colloid Polym. Sci.* **272**, 1611–1619.
22. Shang, T., Smith, K. A., and Hatton, T. A. (2003) Photoresponsive surfactants exhibiting unusually large, reversible surface tension changes under varying illumination conditions, *Langmuir* **19**, 10764–10773.
23. Le Ny, A.-L. M., and Lee, C. T., Jr. (2006) Photoreversible DNA condensation using light-responsive surfactants, *J. Am. Chem. Soc.* **128**, 6400–6408.
24. Glinka, C. J., Barker, J. G., Hammouda, B., Krueger, S., Moyer, J. J., and Orts, W. J. (1998) The 30 m small-angle neutron scattering instruments at the National Institute of Standards and Technology, *J. Appl. Crystallogr.* **31**, 430–445.
25. Guinier, A., and F., G. (1955) *Small Angle Scattering of X-ray*, Wiley, New York.
26. Svergun, D. I. (1992) Determination of the regularization parameter in indirect-transform methods using perceptual criteria, *J. Appl. Crystallogr.* **25**, 495–503.
27. Svergun, D. I., and Koch, M. H. J. (2003) Small-angle scattering studies of biological macromolecules in solution, *Rep. Prog. Phys.* **66**, 1735–1782.
28. Yang, L. (2005) The X21 SAXS instrument at NSLS for studying macromolecular systems, *Macromol. Res.* **13**, 538–541.
29. Chen, S.-H., and Lin, T.-L. (1987) in *Neutron Scattering* (Price, D. L., and Sköld, K., Eds.) pp 489–543, Academic Press, San Diego.
30. Pedersen, J. S., Hansen, S., and Bauer, R. (1994) The aggregation behavior of zinc-free insulin studied by small-angle neutron scattering, *Eur. Biophys. J.* **22**, 379–389.
31. Shilton, B. H., McDowell, J. H., Smith, W. C., and Hargrave, P. A. (2002) The solution structure and activation of visual arrestin studied by small-angle X-ray scattering, *Eur. J. Biochem.* **269**, 3801–3809.
32. Ramakrishna, T., and Pandit, M. W. (1992) Involvement of active site in self-association of proteins: a case of alpha-chymotrypsin, *Indian J. Biochem. Biophys.* **29**, 192–200.
33. Pandit, M. W., and Rao, M. S. N. (1975) Self-association of proteins. Self-association of  $\alpha$ -chymotrypsin at its isoelectric point in buffer solutions of ionic strength 0.1, *Biochemistry* **14**, 4106–4110.
34. Ackers, G. K., and Thompson, T. E. (1965) Determination of stoichiometry and equilibrium constants for reversibly associating systems by molecular sieve chromatography, *Proc. Natl. Acad. Sci. U.S.A.* **53**, 342–349.
35. Svergun, D. I., Richard, S., Koch, M. H. J., Sayers, Z., Kuprin, S., and Zaccai, G. (1998) Protein hydration in solution: experimental observation by X-ray and neutron scattering, *Proc. Natl. Acad. Sci. U.S.A.* **95**, 2267–2272.
36. Durchschlag, H., and Zipper, P. (1996) Comparative determination of structural parameters and conformational changes of proteins by small-angle scattering, crystallography and hydrodynamic analysis, *J. Mol. Struct.* **383**, 223–229.
37. Ninio, J., Luzzati, V., and Yaniv, M. (1972) Comparative small-angle X-ray scattering studies on unacylated, acylated, and crosslinked *Escherichia coli* transfer RNAIva1, *J. Mol. Biol.* **71**, 217–229.
38. Berret, J.-F., and Oberdisse, J. (2004) Electrostatic self-assembly in polyelectrolyte-neutral block copolymers and oppositely charged surfactant solutions, *Phys. B: Condensed Matter (Amsterdam)* **350**, 204–206.
39. Perkins, S. J., Smith, K. F., Kilpatrick, J. M., Volanakis, J. E., and Sim, R. B. (1993) Modelling of the serine-proteinase fold by X-ray and neutron scattering and sedimentation analyses: occurrence of the fold in factor D of the complement system, *Biochem. J.* **295** (Part 1), 87–99.
40. Fujisawa, T., Ueki, T., Inoko, Y., and Kataoka, M. (1987) X-ray scattering from a troponin C solution and its interpretation with a dumbbell-shaped-molecule model, *J. Appl. Crystallogr.* **20**, 349–355.
41. Tranier, S., Mortier-Barriere, I., Ilbert, M., Birck, C., Iobbi-Nivol, C., Mejean, V., and Samama, J.-P. (2002) Characterization and multiple molecular forms of TorD from *Shewanella massilia*, the putative chaperone of the molybdoenzyme TorA, *Protein Sci.* **11**, 2148–2157.
42. Chiti, F., Webster, P., Taddei, N., Clark, A., Stefani, M., Ramponi, G., and Dobson, C. M. (1999) Designing conditions for in vitro formation of amyloid protofilaments and fibrils, *Proc. Natl. Acad. Sci. U.S.A.* **96**, 3590–3594.
43. Vanhoudt, J., Abgar, S., Aerts, T., and Clauwaert, J. (2000) A small-angle X-ray solution scattering study of bovine  $\alpha$ -crystallin, *Eur. J. Biochem.* **267**, 3848–3858.
44. Jaikaran, E. T. A. S., Higham, C. E., Serpell, L. C., Zurdo, J., Gross, M., Clark, A., and Fraser, P. E. (2001) Identification of a novel human islet amyloid polypeptide  $\beta$ -sheet domain and factors influencing fibrillogenesis, *J. Mol. Biol.* **308**, 515–525.
45. Zurdo, J., Guijarro, J. I., Jimenez, J. L., Saibil, H. R., and Dobson, C. M. (2001) Dependence on solution conditions of aggregation and amyloid formation by an SH3 domain, *J. Mol. Biol.* **311**, 325–340.
46. Pallares, I., Vendrell, J., Aviles, F. X., and Ventura, S. (2004) Amyloid fibril formation by a partially structured intermediate state of  $\alpha$ -chymotrypsin, *J. Mol. Biol.* **342**, 321–331.
47. Susi, H., and Byler, D. M. (1986) Resolution-enhanced Fourier transform infrared spectroscopy of enzymes, *Methods Enzymol.* **130**, 290–311.

48. Byler, D. M., and Susi, H. (1986) Examination of the secondary structure of proteins by deconvolved FTIR spectra, *Biopolymers* 25, 469–487.
49. Klunk, W. E., Jacob, R. F., and Mason, R. P. (1999) Quantifying amyloid by Congo red spectral shift assay, *Methods Enzymol.* 309, 285–305.
50. Glenner, G. G. (1980) Amyloid deposits and amyloidosis. I. The  $\beta$ -fibrilloses, *N. Engl. J. Med.* 302, 1283–1292.
51. Puchtler, H., and Sweat, F. (1965) Congo red as a stain for fluorescence microscopy of amyloid, *J. Histochem. Cytochem.* 13, 693–694.
52. Krebs, M. R. H., Bromley, E. H. C., Rogers, S. S., and Donald, A. M. (2005) The mechanism of amyloid spherulite formation by bovine insulin, *Biophys. J.* 88, 2013–2021.
53. Wang, D., Bode, W., and Huber, R. (1985) Bovine chymotrypsinogen A. X-ray crystal structure analysis and refinement of a new crystal form at 1.8 Å resolution, *J. Mol. Biol.* 185, 595–624.
54. Rao, M. S. N., and Kegeles, G. (1958) An ultracentrifuge study of the polymerization of  $\alpha$ -chymotrypsin, *J. Am. Chem. Soc.* 80, 5724–5729.
55. Egan, R., Michel, H. O., Schlueter, R., and Jandorf, B. J. (1957) Physicochemical investigation of the chymotrypsins. II. On the mechanism of dimerization of chymotrypsin, *Arch. Biochem. Biophys.* 66, 366–373.
56. Ding, F., and Dokholyan, N. V. (2005) Simple but predictive protein models, *Trends Biotechnol.* 23, 450–455.
57. Dokholyan, N. V. (2006) Studies of folding and misfolding using simplified models, *Curr. Opin. Struct. Biol.* 16, 79–85.

BI700233K